

Journal Pre-proof

Sol-gel Ni/ γ -Al₂O₃ material as secondary catalyst for toluene reforming: Tailoring the γ -Al₂O₃ substrate with stearic acid

Vincent Claude, Julien Mahy, Francesca Micheli, Jérémy Geens, Stéphanie D. Lambert

PII: S1387-1811(19)30538-4

DOI: <https://doi.org/10.1016/j.micromeso.2019.109681>

Reference: MICMAT 109681

To appear in: *Microporous and Mesoporous Materials*

Received Date: 26 July 2019

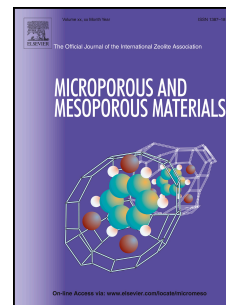
Revised Date: 26 August 2019

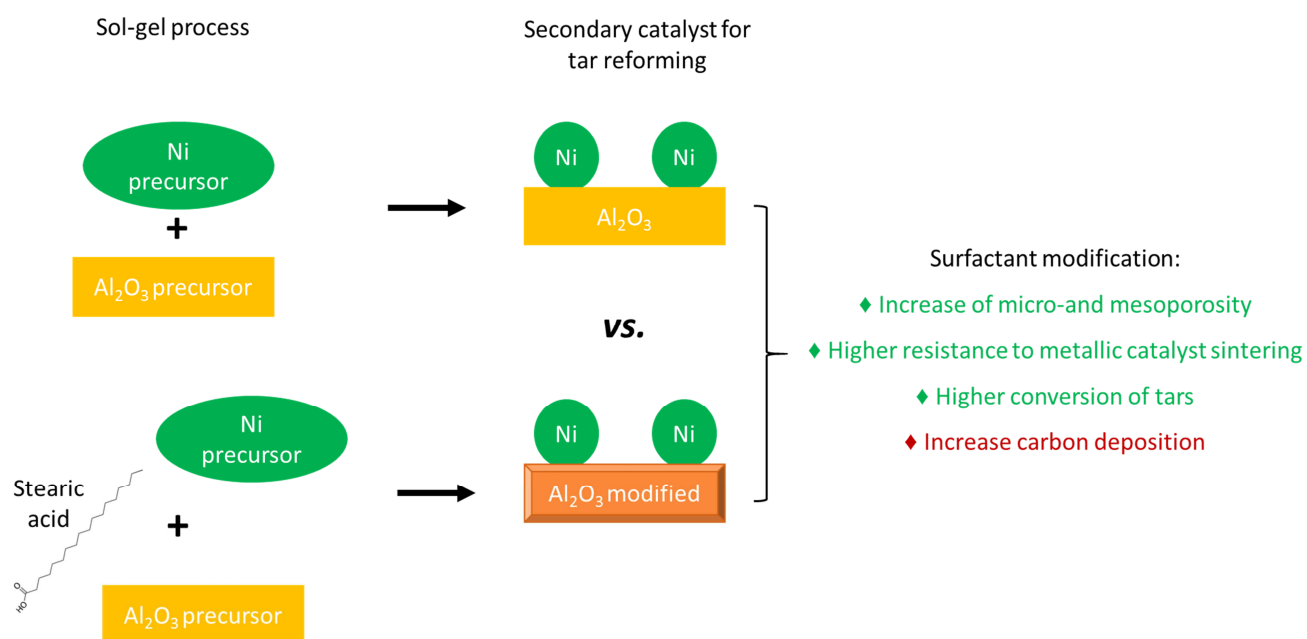
Accepted Date: 26 August 2019

Please cite this article as: V. Claude, J. Mahy, F. Micheli, J. Geens, Sté.D. Lambert, Sol-gel Ni/ γ -Al₂O₃ material as secondary catalyst for toluene reforming: Tailoring the γ -Al₂O₃ substrate with stearic acid, *Microporous and Mesoporous Materials* (2019), doi: <https://doi.org/10.1016/j.micromeso.2019.109681>.

This is a PDF file of an article that has undergone enhancements after acceptance, such as the addition of a cover page and metadata, and formatting for readability, but it is not yet the definitive version of record. This version will undergo additional copyediting, typesetting and review before it is published in its final form, but we are providing this version to give early visibility of the article. Please note that, during the production process, errors may be discovered which could affect the content, and all legal disclaimers that apply to the journal pertain.

© 2019 Published by Elsevier Inc.





Sol-gel Ni/ γ -Al₂O₃ material as secondary catalyst for toluene reforming: Tailoring the γ -Al₂O₃ substrate with stearic acid

Vincent Claude¹, Julien Mahy^{1, 2 *}, Francesca Micheli³, Jérémy Geens¹, Stéphanie D. Lambert¹

¹ *Department of Chemical Engineering – Nanomaterials, Catalysis & Electrochemistry, University of Liège, B6a, Quartier Agora, Allée du six Août 11, 4000 Liège, Belgium*

² *Institute of Condensed Matter and Nanosciences (IMCN), Université catholique de Louvain, Place Louis Pasteur 1, 1348, Louvain-la-Neuve, Belgium*

³ *Department of Industrial Engineering, University of L'Aquila, 18 via G. Gronchi, 67100 L'Aquila, Italy*

***Corresponding author:** Julien G. Mahy, Institute of Condensed Matter and Nanosciences (IMCN), Université catholique de Louvain, Place Louis Pasteur 1, 1348, Louvain-la-Neuve, Belgium. E-mail address: julien.mahy@uclouvain.be.

Keywords: Ni-doped Al₂O₃ catalyst; toluene reforming; Sol-Gel process, mesoporous structure.

Abstract

In this work, Ni-based catalysts supported on alumina were studied for toluene reforming with a particular attention on the substrate texture. Indeed, the influence of stearic acid addition during the synthesis process of Ni/Al₂O₃ catalysts was study on the material texture and catalytic activity. All the samples were also characterized thanks to nitrogen adsorption-desorption isotherm measurements, mercury porosimetry and X-ray diffraction. It

was shown that the step of addition of the surfactant during the synthesis process and the composition of the solvent medium (water/ethanol vs. pure ethanol) strongly modified the texture of the samples. Indeed, the sample prepared with addition of stearic acid before the precipitation step and inside a pure ethanol medium showed the highest increase of micro- and mesoporosity. The modification of the textural properties also proved to influence the size of the Ni particles, and thus the reducibility of the catalysts. The sample which showed the most interesting textural properties was tested for the reforming of 24.000 ppmv of toluene at 650 °C. Results showed that the conversion of toluene strongly increased when the samples were tailored but these changes also increased the catalyst sensitivity to carbon contamination.

1. Introduction

Nowadays, the biomass gasification appears as an interesting and versatile way to produce bio-syngas, which can either be used directly as combustible or converted into storable and high valuable chemical compounds such as methanol [1–3]. However, bio-syngas reactors still encounter some technical problems, which seriously hinder their commercial development [2,4,5]. Indeed, the main problems come from the high tars formation which accumulate in the outlet gas and can condensate, clogging the pipes. Modifications of the gasifier reactor design and of the gasification operating conditions (temperature, space ratio, gasifying reagent) have proved to substantially reduce the tar concentration [2,3,6–9].

Many studies have highlighted the fact that the tar elimination via catalytic reforming seems to be the more practical and economical solution [2,4,9–15]. The required properties of the catalysts are determined by its location: inside the reactor (primary catalyst) or outside the reactor (secondary catalyst). Primary catalysts are generally robust, non-toxic, cheap materials and they are almost only intended for fluidized bed reactors. Secondary catalysts are more

versatile and can be used at the exit of both fluidized and fixed bed reactors. They are characterized by tailored mesoporous shapes, controlled active site dispersion and adapted elemental compositions. In this work, we decided to focus on designing materials for secondary catalytic applications, *i.e.* working at relatively low temperature (~ 650 °C) with no mechanical stress.

Although widely used industrially, Ni is not the most effective catalyst for steam reforming. However, it is the element showing the most interesting activity/price ratio compared to the other more precious metals such as Ru or Rh [2,4]. The optimum Ni loading is situated around 15 wt. % for impregnated and 20 wt. % for precipitated catalysts [9].

These catalysts are commonly supported on Al_2O_3 , ZrO_2 , Zeolites or Olivine. Various studies agree on the fact that $\gamma\text{-Al}_2\text{O}_3$ seems to be the best support for secondary catalyst applications [2,10,15–18]. $\gamma\text{-Al}_2\text{O}_3$ appears to be an interesting support because of its large specific surface area (200-500 m^2/g), high mechanical strength and good sintering resistance. Different methods of preparation are possible for this substrate but the two most common catalyst preparation methods are the incipient wetness impregnation and the sol-gel process. It appears that due to weaker active site/support interactions, the metallic nanoparticles from impregnated catalysts are more inclined to sinter and submit coke deactivation, especially by carbon whiskers formation. Although generally showing lower activity, sol-gel synthesized catalysts are therefore more interesting in terms of lifetime [2,4,19–21]. Furthermore, sol-gel process allows an easy tailoring of the material by adjusting different parameters during synthesis and preparation such as pH, temperature, reactants ratio [22–25].

In this work, we will focus on the catalyst texture modification by the addition of surfactants. Indeed, surfactants are interesting molecules as their dual hydrophilic/hydrophobic character leads to the formation of a locally organized structure (micelles, cylinders ...) that may assemble into larger structures called lyotropic phases

(hexagonal structure, lamellar structure, micellar cubic ...) [26,27]. The lyotropic phases may act as soft template during the gelation of a sol, *i.e.* they prevent gelation where they are located and leave corresponding voids upon removal by heat treatment. Hence, tailoring the gel porosity at the mesoscale becomes possible and has been reported for alumina in previous studies [28,29]. Nevertheless, it was observed that the surfactants do not systematically lead to uniform and regular pore shapes by formation of micelles (for example honeycomb structure). Indeed, it was shown that the surfactant may also be adsorbed onto charged alumina crystallite surfaces, which results in structures without a direct link to the theoretical micelle shapes [30]. The two more common types of surfactants used for the tailoring of alumina are linear carboxylic acids, such as stearic acid, lauric acid or caproic acid [28,31,32], or block copolymers, such as Pluronic P123[®] or Pluronic F127[®] [29,33–35].

In other studies, other surfactants or organic molecules were also used during synthesis for Al₂O₃ tailoring as citric acid [36], triethanolamine [37], cetyltrimethylammonium bromide (CTAB) [38,39] or polyethylene glycol (PEG) [38]. These works showed an increase of the specific surface area with the surfactant addition [38,39], a better dispersion of metal species when high surface specific Al₂O₃ is used as support [39], a link between the resulting Al₂O₃ particle shape and the nature of the surfactant [36,38] and also the influence of the surfactant amount on the pore morphology [35]. The introduction of organic additive is a powerful tool to tailor the Al₂O₃ material [35–39].

In this work, the influence of stearic acid addition in Ni/ γ -Al₂O₃ catalyst will be studied on the material texture and catalytic activity. The stearic acid/Al molar ratio will be set in reference to the work of Kim *et al.* [28] who performed the synthesis of γ -Al₂O₃ supports in similar conditions as the synthesis procedure used in this work in terms of solvent, *pH* and temperature range. However, in the quoted work, Al-tri-*Sec*-butoxide was used as aluminum source. In contrary, in the present work, in order to develop a common and easy aqueous sol-

gel method for the synthesis of surfactant modified Ni/ γ -Al₂O₃ catalysts, Al(NO₃)₃ was used as aluminum source. The influence of surfactant addition will be studied thanks to nitrogen adsorption-desorption isotherm measurements, mercury porosimetry and X-ray diffraction. Finally, the sample which showed the most interesting textural properties will be tested for the reforming of 24.000 ppmv of toluene at 650 °C.

2. Materials and Methods

2.1. Synthesis of Ni/ γ -Al₂O₃ catalysts modified with stearic acid

In order to match with the procedures applied by Kim *et al.*[28], the amount of stearic acid used was set to a “surfactant/Al” molar ratio equal to 0.2. Figure 1 depicts the different methods (A to E) used to prepare the samples. In all cases, the same amount of Ni is added (10 wt.%). The first method (method A) concerns the reference sample without surfactant addition. The reference sample was synthesized according to a synthesis procedure described in [40]. First, aluminum precursor (aluminum nitrate, Al(NO₃)₃.9H₂O, \geq 98%, Sigma Aldrich), ethanol and water were mixed together. Then, the sol was formed by a slow addition of a NH₄OH solution (30 wt. %, 15 M). After precipitation, the sol was agitated for 24 h at 85 °C, washed two times with water, re-dispersed in water and nickel nitrate hexahydrate (Ni(NO₃)₂.6H₂O, 99.99%, Sigma Aldrich) was added. The sol was stirred for 30 min. The doped sol was put in an oven for aging (24 h, 85 °C, 700 mbar) and for drying (24 h, 110 °C, 900 mbar). The dried gel was calcined for 5 h at 550 °C, with a heating rate of 2 °C/min. Ni10/Al₂O₃-A sample is produced.

In the case of the sample prepared by the method B, the stearic acid was added at the same time as the aluminum precursor (Figure 1 (B)). The solution was stirred for 30 min and the precipitation was performed with NH₄OH. After the washing steps, the sol was dispersed

in a media of water/ethanol, doped with nickel nitrate, stirred for 30 min, put in oven for drying and calcined at 550 °C. This method was used for the preparation of Ni10/Al₂O₃-B sample. The method C was similar, except that instead of using a water/ethanol media in the initial solution, pure ethanol was used (Figure 1 (C)). This method was used for the preparation of Ni10/Al₂O₃-C sample.

In the case of samples prepared by the method D (Figure 1 (D)), the boehmite (AlOOH) sol was prepared according to the standard procedure used for the preparation of reference sample [40]. After being washed, the sol was redispersed in the water/ethanol medium. First, nickel nitrate was added, followed by the stearic acid. The sol was stirred for 30 min, put in an oven for drying and calcined at 550 °C. This method was used for the preparation of Ni10/Al₂O₃-D sample. The method E was similar, except that instead of using a water/ethanol medium in the dispersed solution, pure ethanol was used (Figure 1 (E)). This method was used for the preparation of Ni10/Al₂O₃-E sample.

The amount of reagents were denoted in Supplementary Materials in Table S1.

2.2. Characterizations

Samples compositions are determined by inductively coupled plasma–atomic emission spectroscopy (ICP–AES), equipped with an ICAP 6500 THERMO Scientific device. Solid samples are crushed and then dissolved with lithium tetraborate before analysis. Aluminum, and nickel loadings are obtained by comparison with standard solutions in the same medium.

Textural properties are determined thanks to nitrogen adsorption-desorption isotherms which are measured at -196 °C on a Micromeritics ASAP 2010 instrument after 12 h of outgassing at 300 °C and 10⁻⁵ Pa. The microporous volume, V_{DR} , is calculated by the Dubinin-Raduskevitch method on the first branch of the adsorption curves at low relative pressure

($p/p_0 < 0.4$). The pore size distributions are determined by the Broekhoff de Boer method (BdB) applied to the adsorption profil-branch of the nitrogen isotherm [41].

Mercury porosimetry measurements were performed on monoliths samples crushed between 300 and 700 μm using a Poremaster60 instrument from Quantachrome with pressures going from 1 to 60.000 Psi. The measurements allowed determining the macroporous volume (V_{Hg} , cm^3/g), to plot the curves of volume introduced as a function of the pressure and to plot the macropore size distribution.

Apparent densities, ρ_{app} , were measured by helium pycnometry by using a Micromeritics AccuPyc 1330 device. The density was determined from an average of six consecutive measurements. According to IUPAC recommendations for the characterization of porous solids, the apparent density of an object is defined as the density of that object including closed pores [42]. The effective density or true density, ρ_{Eff} , in g/cm^3 , is defined as the density of an object excluding pores. The ρ_{Eff} values were calculated by dividing the mass of the catalyst bed by the catalytic bed volume inside the quartz tube ($\text{Ø} = 8 \text{ mm}$, $h = 12 \text{ mm}$), for sieved grains (average Ø of 500 μm) and assuming that the grains were sphere-like and closed-packed at the highest ratio (0.74).

The crystallographic properties of the samples were determined by X-ray diffraction on a Siemens D5000 diffractometer (Cu-K_α radiation) between 30° and 80° (2θ) with a step time of 18 s and a step size of 0.04° . The alumina crystallites sizes were calculated by using the Scherrer equation centered on the (4 0 0) ray of $\gamma\text{-Al}_2\text{O}_3$ ($2\theta = 67.0^\circ$) on the XRD pattern. The $\text{Ni}^{(0)}$ crystallites sizes were calculated by using the Scherrer equation centered on the (2 0 0) ray ($2\theta = 51.83^\circ$).

The size of metallic particles and their distribution were measured by transmission electron microscopy (TEM) performed on a CM10-PW6020 Philips Electron Microscope by

averaging the measurement of approximately 100 particles on TEM micrographs. First, crushed samples were dispersed in absolute ethanol. Then a drop of the dispersion was placed on a copper grid (Formvar/Carbon 200 Mesh Cu from Agar Scientific).

Scanning Electron Microscopy measurements were performed with a FEI ESEM-FEG XL3 device. Pictures made with Backscattered Electron (SEM-BSE) detectors allowed getting a view of the surface of the samples, with different contrasts depending on the elemental composition. The measurements were performed at an acceleration voltage of 15 keV, set on the Spot 4 and with a vacuum of 0.4 Torr. No previous metallization of the samples was necessary.

H₂ reduction steps were performed on 1 g of sample. The reactor was first purged with He at room temperature (15 min, 50 mL/min), then H₂ was sent to the sample (50 mL/min) and the temperature was increased (from 25 °C to 750 °C with a heating rate of 5 °C/min). After 1 h at 750 °C, the heating was stopped and the reactor was purged with He (50 mL/min).

Temperature Programmed Reduction measurements were performed with a TPD/R/O 1100 device from CE instruments to give information about the reduction of the metallic species (Ni or Fe) present in the samples. An amount of 0.2 g of catalyst was put in a quartz tube. Samples were heated from 25 °C to 1000 °C with a heating rate of 2 °C/min and under a flow of 20 mL/min of a gas mixture (5 % vol. H₂/95 % vol. N₂).

After the catalytic tests, carbon deposits were studied with thermogravimetric (TG) and differential scanning calorimetry (DSC) measurements, which are realized with a Sensys Setaram instrument. Samples are heated from 25 to 800 °C with a heating rate of 2 °C/min under air flow (20 mL/min).

2.3. Catalytic experiments

The samples were tested at 650 °C, for 300 min, with a standard procedure described in [43,44], with a toluene concentration of 24.000 ppmv and a gas mixture of 31.5 %vol. H₂, 31.5 %vol. CO, 15.2 %vol. CO₂, 11 %vol. H₂O, 10 %vol. CH₄. The mass of the catalyst was set to 300 mg, for a catalytic bed height of 12 mm, with a gas flowrate of 50 mL/min and consequently a *GHSV* of 5000 h⁻¹ (residence time of 0.72 sec).

The toluene conversion, C_T , was determined from the Equation 1:

$$C_T = \frac{C_{T,In} - C_{T,Out}}{C_{T,In}} * 100 \quad (1)$$

where $C_{T,in}$ is the initial toluene concentration (mol/m³) and $C_{T,out}$ is the toluene concentration at the outlet of the reactor (mol/m³).

The benzene selectivity, S_B , was determined from the Equation 2:

$$S_B = \frac{C_{B,Out}}{C_{T,In} - C_{T,Out}} * 100 \quad (2)$$

where $C_{B,Out}$ is the outlet concentration of benzene (mol/m³), $C_{T,in}$ is the initial toluene concentration (mol/m³) and $C_{T,Out}$ is the toluene concentration at the outlet of the reactor (mol/m³).

The methane conversion, C_{CH_4} , was determined from the Equation 3:

$$C_{CH_4} = \frac{C_{CH_4,In} - C_{CH_4,Out}}{C_{CH_4,In}} * 100 \quad (3)$$

where $C_{CH_4,In}$ is the initial methane concentration (mol/m³) and $C_{CH_4,Out}$ is the methane concentration at the outlet of the reactor (mol/m³).

All C_T , S_B and C_{CH_4} values were obtained by making an average of the results obtained during the last 10 measurements of each test.

The consumption rate of toluene, r_T , in $\text{mol}_T/(\text{g}_{Ni}\cdot\text{h})$, was also compared. For this gas mixture, the $(\text{H}_2\text{O} + \text{CO}_2)/\text{C}$ ratio is about 1.6 when only taking toluene as carbon source, and it is about 1.0 when taking toluene + methane as carbon source. Though these values are low, they are equal or higher to the stoichiometric ratio. Hence, the toluene consumption rate can be expressed with respect only to the toluene concentration and according to a first order reaction ($n = 1$), which leads to:

$$-r_T = k \cdot C_{\text{Tolu}} \quad (4)$$

where r_T is the consumption rate of toluene ($\text{mol}_T/(\text{g}_{Ni}\cdot\text{h})$), k is the apparent kinetic constant ($\text{m}^3/(\text{g}_{Ni}\cdot\text{h})$) and C_{Tolu} is the concentration of toluene ($\text{mol}_{\text{Tolu}}/\text{m}^3$).

Since the reaction rate is assumed to be of first order ($n = 1$), r_T can also be expressed as follows [45,46]:

$$r_T = \left(-\frac{F_T}{W}\right) \ln(1 - f_T) \quad (5)$$

where F_T is the molar flowrate of toluene at the reactor inlet (mol_T/h), W is the nickel mass inside the reactor (g) and f_T is the toluene conversion ($f_T = C_T/100$).

In order to get a more accurate comparison of the coking tendency of the catalysts, the term *Coke** was introduced. This value corresponds to the amount of carbon formed by gram of toluene converted and is determined by Equation 6:

$$Coke^* = \frac{Coke}{r_T * \left(\frac{\%Ni}{100}\right) * t * M_T} \quad (6)$$

where *Coke* is the amount of carbon deposit determined from TG-DSC measurements ($\text{g}_{\text{Carbon}}/\text{g}_{\text{Cata}}$), ($\%Ni/100$) is the gram of nickel per gram of catalyst, determined from ICP-AES measurements, r_T is the consumption rate of toluene ($\text{mol}_{\text{Tolu}}/(\text{g}_{\text{Ni}}\cdot\text{h})$), t is the time of test (5 h) and M_T is the molecular mass weight of toluene (92.1 g/mol).

According to calculation presented in Supplementary Materials, it was assumed that all samples did not submit neither internal nor external diffusional limitations during the catalytic tests.

3. Results and Discussion

3.1. Influence of the stearic acid addition on catalyst morphology and texture

Table 1 shows the theoretical and actual compositions of the samples. All samples presented similar theoretical and actual compositions.

In Figure 2, TEM pictures show that all samples present similar morphology at nanoscale and that the addition of the surfactant do not cause any visible modifications of the alumina crystallites sizes, of their morphology or of the arrangement of the aggregates.

The nitrogen adsorption-desorption isotherms and the associated mesopore size distribution of the samples are presented in Figure 3. The textural properties (S_{BET} , V_p and V_{DR}) and the sizes of the alumina crystallites obtained by X-Ray diffraction ($d_{\text{XRD,Al}_2\text{O}_3}$) are presented in Table 1. It was observed that the sizes of the $\gamma\text{-Al}_2\text{O}_3$ crystallites ($d_{\text{XRD,Al}_2\text{O}_3}$) are similar for all samples. This observation is in accordance with the TEM observations (Figure 2), for which the addition of stearic acid do not influence the morphology and size of the $\gamma\text{-Al}_2\text{O}_3$ crystallites.

Table 1 reveals that the textural properties (S_{BET} , V_{p} and V_{DR}) increase for all samples synthesized with stearic acid. For both solvent media (pure ethanol or water/ethanol mixture), the addition of the surfactant before the precipitation step (method B) allows a deeper modification of the textural properties of the samples compared to an addition of the surfactant after the agitation step (method D). In this way, in comparison to reference sample, Ni10/Al₂O₃-B sample shows a higher increase of its textural properties ($\Delta S_{\text{BET}} = + 75 \text{ m}^2/\text{g}$, $\Delta V_{\text{p}} = + 0.5 \text{ cm}^3/\text{g}$, $\Delta V_{\text{DR}} = + 0.04 \text{ cm}^3/\text{g}$) compared to Ni10/Al₂O₃-D sample ($\Delta S_{\text{BET}} = + 40 \text{ m}^2/\text{g}$, $\Delta V_{\text{p}} = + 0.2 \text{ cm}^3/\text{g}$, $\Delta V_{\text{DR}} = + 0.02 \text{ cm}^3/\text{g}$). Similar trends are observed when comparing the textural values between samples Ni10/Al₂O₃-A, Ni10/Al₂O₃-C and Ni10/Al₂O₃-E.

Since no regular structuration of the alumina support is observed by TEM measurements and that $d_{\text{XRD,Al}_2\text{O}_3}$ values are similar for all samples, it is assumed that the stearic acid molecules are more inclined to be adsorbed on the surface of the boehmite (AlOOH) crystallites rather than forming separated micelles [30]. In this way (Figure 4), in the case of the addition of the surfactant before the precipitation step (Ni10/Al₂O₃-B and Ni10/Al₂O₃-C), the alumina hydroxide crystallites are fully covered by the stearic acid molecules as soon as they begin to form (Figure 4a). During the drying step, the presence of these molecules prevents a compact aggregation of the crystallites, which resulted in an increase of the micro- and mesoporosity of the samples after calcination. In contrary, when the surfactant is added after the agitation time (Ni10/Al₂O₃-D and Ni10/Al₂O₃-E samples), it is assumed that the boehmite crystallites are already partially agglomerated (Figure 4b). Consequently, the chains of stearic acid molecules present more difficulties to cover the surface of the boehmite crystallites, which results in a lower modification of the textural properties of the samples.

It is observed in Table 1 that the use of pure ethanol instead of “water/ethanol” mixture as solvent medium lead to samples with similar V_{DR} and S_{BET} values. Nevertheless, the porous

volume at saturation pressure of nitrogen, V_p , is higher when pure ethanol is used as solvent. Despite the total volume of solvent being established in both cases to totally dissolve the stearic acid, the variations of V_p values could be a consequence of a different dispersion of the surfactant molecules. Indeed, the solubility of stearic acid is clearly higher in ethanol than in water ($solubility_{Ethanol,25^\circ C} = 3.16 \text{ g}_{Surfactant}/\text{g}_{Ethanol}$ whereas $solubility_{H_2O,25^\circ C} = 0.034 \text{ g}_{Surfactant}/\text{g}_{H_2O}$). Hence, a higher solubility do not apparently influence the covering of the alumina crystallites (no higher V_{DR}), but could favor the formation of micelles, which would explain the increase of V_p . Based on the data presented in Table 1, Figure 5 plots the metallic nickel particles sizes (calculated by doing an average of d_{TEMNi} and d_{XRDNi} values) for all samples as a function of the microporous volume, V_{DR} . It was observed that the samples with the highest microporous volume (Ni10/Al₂O₃-B and Ni10/Al₂O₃-C samples) present the lowest initial Ni particles sizes (Figure 5a) and the lowest trend to sinter (Figure 5b). This observation confirms the fact that the sintering of the metallic Ni particles occurs via a mechanism of crystallite migration, and that they are strongly affected by the support microposity [18,47].

Figure 6 shows the TPR profiles of the Ni/ γ -Al₂O₃ samples modified with stearic acid. It is observed that, though being composed of Ni and γ -Al₂O₃ in similar ratios and prepared with the same operating variables, the samples presented different reduction profiles. This could be a consequence of their different initial nickel oxide particles sizes. Indeed, smaller nickel oxide particles could led to stronger interactions with the γ -Al₂O₃ support, and consequently delay the reduction of nickel oxide by the formation of spinelles like NiAl₂O₄ for example [48,49]. On small particles there are a very important electron density which gives a very strong metal-oxygen bond, more difficult to reduce. One other factor which can also affect the reducibility of the catalysts is the initial oxide composition which can affect its interaction with Al₂O₃.

In Figure 6, it is observed for Ni10/Al₂O₃-D sample that the maximal reduction peak value is not changed ($T \sim 850$ °C), but that the peak is broadened ($T = 600-1000$ °C). By comparison to Ni10/Al₂O₃-A sample, the use of stearic acid in Ni10/Al₂O₃-D sample could led to larger dispersion of initial Ni oxide particle sizes and explains the shift of the H₂ consumption peak towards lower temperatures ($T = 600-700$ °C) and higher temperatures ($T = 900-1000$ °C). The broadening of the peak could be also a consequence of the formation of NiAl₂O₄ spinelles, more difficult to reduce by their high interactions with the support [43,44,48].

For Ni10/Al₂O₃-E sample (Figure 6), the reduction peak is also broadened from 600 °C to 1000 °C. Furthermore, the maximal reduction peak is shifted towards higher temperatures compared to Ni10/Al₂O₃-A and Ni10/Al₂O₃-D samples ($\Delta T = + 60$ °C). The broadening of the peak can be explained by the initial presence of nickel oxide particles with different sizes since this sample shows the highest TEM standard deviation after TPR ($\sigma_{\text{TEM}} = 14$ nm) (Table 1), and by the presence of different nickel oxide species (NiO, NiAl₂O₄,...) with different interactions with the alumina support. Since Ni10/Al₂O₃-E sample presents a higher porous volume, V_p , than Ni10/Al₂O₃-A and Ni10/Al₂O₃-D samples, it is assumed that the presence of a higher V_p would favor the formation of larger initial nickel oxide particles and would also favor the formation of larger metallic particles by sintering.

In Figure 6, Ni10/Al₂O₃-B and Ni10/Al₂O₃-C samples show centered reduction peaks, which are shifted towards lower temperatures ($T \sim 780$ °C). Both samples show the highest V_{DR} and V_p values and lowest metallic Ni particles sizes with small standard deviation ($\sigma_{\text{TEM}} = 6$ nm) after TPR measurements (Table 1). However, Ni10/Al₂O₃-C sample, which presents a slightly higher V_p value, shows larger metallic particle sizes after TPR measurements compared to Ni10/Al₂O₃-B sample (for Ni10/Al₂O₃-B, $d_{\text{TEMNi}} = 16$ nm and $d_{\text{XRDNi}} = 16$ nm; whereas for Ni10/Al₂O₃-C: $d_{\text{TEMNi}} = 24$ nm and $d_{\text{XRDNi}} = 19$ nm) (Table 1).

In view of these results, the following assumptions are strengthened: i) larger initial Ni oxide particles lead to broadened reduction peaks; ii) an increase of the microporosity of the alumina support allows preventing the sintering of the metallic particles at high temperatures; iii) an increase of the mesoporous volume of the alumina support without an adequate microporous volume favors the formation of larger metallic particles with broad distribution of sizes.

Ni10/Al₂O₃-C sample is selected for further characterizations and catalytic tests because it shows the highest V_p value, a high V_{DR} value, and a symmetric H₂ consumption peak, which is shifted towards lower temperatures during TPR measurement.

3.2.. Further textural properties of Ni10/Al₂O₃-C catalyst

Figures 7 shows the microscopic aspect of Ni10/Al₂O₃-A sample (Figure 7a) and Ni10/Al₂O₃-C sample at different scales (Figures 7b and 7c). Ni10/Al₂O₃-C sample is formed of microscopic grains whose shapes and sizes are similar to Ni10/Al₂O₃-A sample (pure γ -Al₂O₃ supports) [40]. However, whereas Ni10/Al₂O₃-A sample presents a close compaction of their grains and hence a relatively smooth surface, in the case of Ni10/Al₂O₃-C sample, the grains are expanded and the microscopic surface is extremely rough.

Figures 8 shows the mercury porosimetry curves for Ni10/Al₂O₃-A and Ni10/Al₂O₃-C samples. In contrary to Ni10/Al₂O₃-A sample, which shows no macroporosity, Ni10/Al₂O₃-C sample is macroporous with pore sizes comprised between 1 and 10 μm and a macroporous volume, V_{Hg} , equal to 0.9 cm^3/g (Table 1).

It is observed in Table 1 that the apparent density value measured by He pycnometry, ρ , of Ni10/Al₂O₃-C sample is very close to the value of Ni10/Al₂O₃-A sample. However, the effective density value, ρ_{Eff} , which corresponds to the mass of pellets inside the catalyst bed

divided by the volume of catalytic bed with close-packing of 0.74, is very different between the two samples: 0.7 g/cm^3 for Ni10/Al₂O₃-A and 0.2 g/cm^3 for Ni10/Al₂O₃-C.

3.3. Catalytic performances of Ni10/Al₂O₃-C catalyst

Since the effective density, ρ_{eff} , of Ni10/Al₂O₃-C sample is smaller than for the reference catalyst Ni10/Al₂O₃-A (Table 1), the catalytic bed volume and the gas flowrate are kept at standard values, but the mass of the catalyst is set to 100 mg instead of 300 mg. Figure 9 shows the conversion of toluene as a function of time for both samples. It is to remind that since the mass of Ni10/Al₂O₃-A catalyst and the mass of Ni10/Al₂O₃-C catalyst are different, the rigorous comparison of the catalyst activity must only be performed according to their r_T values presented in Table 2.

It is observed in Figure 9 that Ni10/Al₂O₃-C sample presents a high conversion of toluene at its first injection ($C_T = 71 \%$). This is attributed to small initial nickel oxide particles which are easily reduced (see TPR measurements, Figure 6). However, Ni10/Al₂O₃-C sample presents an important and continuous loss of its catalytic activity during the test (between 0 min and 300 min: $\Delta C_T \sim -35 \%$).

Table 2 shows the metallic Ni particles sizes after the catalytic test, and the catalytic performances of the samples. The DSC curves obtained for the two samples after the catalytic test are presented in Figure 10.

In Table 2, Ni10/Al₂O₃-C sample shows a higher r_t value compared to the standard Ni10/Al₂O₃-A sample but within the same range. However, Ni10/Al₂O₃-C sample presents also a very high amount of carbon deposit after test ($C_{\text{Coke}} = 1.35 \text{ g}_{\text{Carbon}}/\text{g}_{\text{Cata}}$), which is mostly constituted of filamentous carbon (Figure 10) [44]. So though the r_T value is multiplied by 2

between Ni10/Al₂O₃-A and Ni10/Al₂O₃-C samples, the *Coke** value is in contrary multiplied by 6.

The catalytic behavior of Ni10/Al₂O₃-C sample is similar to the results obtained previously in [44] for Ni20/Al₂O₃ and Ni10/Al₂O₃-IMP samples. Indeed, NiO, present in samples after the calcination step and reducible at lower temperatures than the catalytic test (650 °C), do not take advantage of the mechanism of “special reduction by toluene” [44], and as consequence is deactivated during the catalytic test. However, the fact that Ni10/Al₂O₃-C sample shows much more sensibility towards coking than Ni20/Al₂O₃ and Ni10/Al₂O₃-IMP samples suggest that other parameters emphasize the formation of carbon.

It is to remind that the reforming of toluene on Ni/Al₂O₃ catalysts occurs according to several reactions, which take place simultaneously, and which is summarized as follows [50–52]:

- i) in a first step, toluene is adsorbed on the surface of the metallic particle and cracked into C_xH_y_{ads} + C_{ads} + H_{ads} species. $r_{T,ads.+crack.}$ is the rate of adsorption and cracking of the toluene molecules;
- ii) in parallel, H₂O and CO₂ molecules are adsorbed on the surface and dissociated into reactive species (O_{ads}, HO_{ads}, H_{ads});
- iii) the reactive oxidant species (O_{ads}, HO_{ads}) react with the carbonaceous compounds (coming from the cracking of toluene) to form CO and H₂ by gasification reactions. $r_{gasification}$ is the rate of gasification of the carbonaceous compounds into CO and H₂.

The cracking of toluene occurs quickly in presence of metallic nanoparticles. In contrary, the mechanism of carbon removal, which includes the dissociation of the H₂O or CO₂ molecules on the surface of the support (alumina), and the diffusion of the oxidant species (O_{ads}, HO_{ads}) from the support surface to the metallic particle, requires a long contact

time [18,53]. In this way, da Silva *et al.* [53] showed that an increase of the *GHSV* (or a decrease of the residence time) could lead to a loss of balance between the cracking of toluene and the gasification reactions at the surface of the metallic nanoparticles (in other terms, $r_{T,ads.+crack.}$ is higher than $r_{gasification}$). It is shown In Supplementary Material, that neither external nor internal diffusional limitations are observed for both samples, which means that these catalysts work under chemical regime [54]. Nevertheless, Ni10/Al₂O₃-C sample presents a more open structure (larger meso- and macropores) than Ni10/Al₂O₃-A sample. As a consequence, it is assumed that the diffusion of the gaseous reagents is better in Ni10/Al₂O₃-C sample compared to Ni10/Al₂O₃-A sample. This better diffusion could explain the higher r_T value observed for Ni10/Al₂O₃-C sample during the catalytic test, but the values stay in the same range. In return, this better diffusion might have destabilized the balance between the cracking ($r_{T,ads.+crack.}$) and the gasification reactions ($r_{gasification}$) at the surface of the Ni⁽⁰⁾ particles, thus explaining why Ni10/Al₂O₃-C sample present very large amounts of carbon deposit compared to Ni10/Al₂O₃-A samples (Table 2). Figure 11 gives an overview of the two different cases.

Finally, it is also assumed that the presence of a broad and large distribution of meso- and macropore sizes for Ni10/Al₂O₃-C sample could favor the growth of filamentous carbon.

4. Conclusions

In this work, the influences of stearic acid addition in Ni/ γ -Al₂O₃ catalyst were studied on the material texture and catalytic activity. Four surfactant-modified Ni/Al₂O₃ catalysts were synthesized by sol-gel process. One Ni/ γ -Al₂O₃ catalyst without stearic acid was produced as reference material.

This paper highlighted that the sol-gel preparation method can efficiently modify the textural properties of 10 wt. % Ni/ γ -Al₂O₃ catalysts thanks to the addition of a common surfactant. It was shown that the step of addition of the surfactant (before precipitation *vs.* after long agitation) and the composition of the solvent medium (water/ethanol *vs.* pure ethanol) had a consequent influence on the texture modification of the samples. In this way, because of a better initial dispersion of the surfactant molecules and a good covering of the boehmite (AlOOH) particles as soon as they were formed, the sample prepared with addition of stearic acid before the precipitation step and inside a pure ethanol medium showed the highest increase of micro- and mesoporosity.

The modification of the textural properties also proved to influence the size of the Ni particles, and thus the reducibility of the 10 wt. % Ni/ γ -Al₂O₃ catalysts. In this way, the samples with high microporosity showed more uniform initial sizes for nickel oxide particles, which were easier to reduce. Furthermore, the high microporous volume afforded a better resistance to the samples against sintering at high temperatures ($T \sim 1000$ °C). In contrary, the samples which showed higher mesoporous values and no adequate microporous values, presented a broader distribution of Ni⁽⁰⁾ particles sizes and broader TPR reduction profiles.

SEM and mercury porosimetry measurements confirmed that the addition of the surfactant modified the macroporosity of the catalyst. The modification of the textural properties proved to be a powerful tool in order to increase the reaction rate of the conversion of toluene. However, it was observed that the catalyst modified with the surfactant showed a progressive deactivation during the catalytic tests and large amounts of carbon deposit after the test. This high trend towards the formation of carbon was partially attributed to the presence of nickel oxides easily reduced, which did not take advantage of the anti-coking effect brought by the mechanism of “special reduction by toluene”. It was also hypothesized that the large macropores did not permit to restrict the formation of filamentous carbon.

Moreover, the high formation of carbon was also attributed to the high diffusion capacity of the catalyst modified with the surfactant, which was assumed to destabilize the ratio between the amount of tar cracked and the amount of carbonaceous compounds gasified by O_{ads} and HO_{ads} reactive species. However, more studies need to be performed in order to get a better understanding of the influence of the texture on the catalytic performances of $Ni/\gamma-Al_2O_3$ catalysts during the reforming of toluene.

Acknowledgements

V. Claude thanks to F.R.S.-F.N.R.S. for his doctoral grant obtained with the “Fonds de Recherche collective” n° 2.4541.12. S. D. L. is also grateful to F.R.S.-F.N.R.S for her Senior Research Associate position. The authors also acknowledge the Ministère de la Région Wallonne Direction Générale des Technologies, de la Recherche et de l’Energie (DGO6) and the Fond de Bay for financial supports.

Compliance with ethical standards

Conflict of interest: The authors declare that they have no conflicts of interest.

References

- [1] B.& B. Gershman, Gasification of Non-Recycled Plastics From Municipal Solid Waste In the United States, GBB report, 2013.
- [2] V. Claude, C. Courson, M. Köhler, S.D. Lambert, Overview and Essentials of Biomass Gasification Technologies and Their Catalytic Cleaning Methods, *Energy and Fuels*. 30 (2016) 8791–8814. doi:10.1021/acs.energyfuels.6b01642.

- [3] V. Claude, C. Courson, M. Köhler, S.D. Lambert, Correction to overview and essentials of biomass gasification technologies and their catalytic cleaning methods (Energy Fuels (2016) 30:11 (8791-8814) DOI: 10.1021/acs.energyfuels.6b01642), Energy and Fuels. 31 (2017) 1050. doi:10.1021/acs.energyfuels.6b03436.
- [4] F.L. Chan, A. Tanksale, Review of recent developments in Ni-based catalysts for biomass gasification, Renew. Sustain. Energy Rev. 38 (2014) 428–438. doi:10.1016/j.rser.2014.06.011.
- [5] M. Qiu, Y. Li, T. Wang, Q. Zhang, C. Wang, X. Zhang, et al., Upgrading biomass fuel gas by reforming over Ni–MgO/ γ -Al₂O₃ cordierite monolithic catalysts in the lab-scale reactor and pilot-scale multi-tube reformer, Appl. Energy. 90 (2012) 3–10. doi:10.1016/j.apenergy.2011.01.064.
- [6] Z.A.B.Z. Alauddin, P. Lahijani, M. Mohammadi, A.R. Mohamed, Gasification of lignocellulosic biomass in fluidized beds for renewable energy development: A review, Renew. Sustain. Energy Rev. 14 (2010) 2852–2862. doi:10.1016/j.rser.2010.07.026.
- [7] I. Narvaez, A. Orio, M.P. Aznar, Biomass Gasification with Air in an Atmospheric Bubbling Fluidized Bed . Effect of Six Operational Variables on the Quality of, Ind.Eng.Chem.Res. 35 (1996) 2110–2120.
- [8] M.L. Salvador, J. Arauzo, R. Bilbao, Catalytic Steam Gasification of Pine Sawdust . Effect of Catalyst Weight / Biomass Flow Rate and Steam / Biomass Ratios on Gas Production and Composition, Energy and Fuels. (1999) 851–859.
- [9] S. Albertazzi, F. Basile, J. Brandin, J. Einvall, C. Hulteberg, M. Sanati, Clean Hydrogen-rich Synthesis Gas, Chrisgas report, 2004.
- [10] S. Anis, Z. a. Zainal, Tar reduction in biomass producer gas via mechanical, catalytic

- and thermal methods: A review, *Renew. Sustain. Energy Rev.* 15 (2011) 2355–2377.
doi:10.1016/j.rser.2011.02.018.
- [11] D. Li, Y. Nakagawa, K. Tomishige, Development of Ni-Based Catalysts for Steam Reforming of Tar Derived from Biomass Pyrolysis, *Chinese J. Catal.* 33 (2012) 583–594. doi:10.1016/S1872-2067(11)60359-8.
- [12] D. Świerczyński, S. Libs, C. Courson, a. Kiennemann, Steam reforming of tar from a biomass gasification process over Ni/olivine catalyst using toluene as a model compound, *Appl. Catal. B Environ.* 74 (2007) 211–222.
doi:10.1016/j.apcatb.2007.01.017.
- [13] J.N. Kuhn, Z. Zhao, A. Senefeld-Naber, L.G. Felix, R.B. Slimane, C.W. Choi, et al., Ni-olivine catalysts prepared by thermal impregnation: Structure, steam reforming activity, and stability, *Appl. Catal. A Gen.* 341 (2008) 43–49.
doi:10.1016/j.apcata.2007.12.037.
- [14] Z. Zhao, N. Lakshminarayanan, J.N. Kuhn, A. Senefeld-Naber, L.G. Felix, R.B. Slimane, et al., Optimization of thermally impregnated Ni–olivine catalysts for tar removal, *Appl. Catal. A Gen.* 363 (2009) 64–72. doi:10.1016/j.apcata.2009.04.042.
- [15] M.M. Yung, W.S. Jablonski, K. a. Magrini-Bair, Review of Catalytic Conditioning of Biomass-Derived Syngas, *Energy & Fuels.* 23 (2009) 1874–1887.
- [16] Z.R. Ismagilov, M.A. Kerzhentsev, V.A. Sazonov, L.T. Tsykoza, N. V Shikina, V. V Kuznetsov, et al., Study of Catalysts for Catalytic Burners for Fuel Cell Power Plant Reformers, *Korean J.Chem Eng.* 20 (2003) 461–467.
- [17] S. Wang, CO₂ reforming of methane on Ni catalysts: Effects of the support phase and preparation technique, *Appl. Catal. B Environ.* 16 (1998) 269–277.

- [18] J. Rostrup-Nielsen, Catalytic Steam Reforming, *Catal. Sci. Technol.* 5 (1984) 1–117. doi:doi.org/10.1007/978-3-642-93247-2_1.
- [19] W.-S. Xia, Y.-H. Hou, G. Chang, W.-Z. Weng, G.-B. Han, H.-L. Wan, Partial oxidation of methane into syngas ($H_2 + CO$) over effective high-dispersed Ni/SiO₂ catalysts synthesized by a sol–gel method, *Int. J. Hydrogen Energy.* 37 (2012) 8343–8353. doi:10.1016/j.ijhydene.2012.02.141.
- [20] Y. Zhang, G. Xiong, S. Sheng, W. Yang, Deactivation studies over NiO/γ-Al₂O₃ catalysts for partial oxidation of methane to syngas, *Catal. Today.* 63 (2000) 517–522.
- [21] L. Zhang, X. Wang, B. Tan, U.S. Ozkan, Effect of preparation method on structural characteristics and propane steam reforming performance of Ni–Al₂O₃ catalysts, *J. Mol. Catal. A Chem.* 297 (2009) 26–34. doi:10.1016/j.molcata.2008.09.011.
- [22] L. Tasseroul, S.L. Pirard, S.D. Lambert, C. a. Páez, D. Poelman, J.P. Pirard, et al., Kinetic study of p-nitrophenol photodegradation with modified TiO₂ xerogels, *Chem. Eng. J.* 191 (2012) 441–450. doi:10.1016/j.cej.2012.02.050.
- [23] J.G. Mahy, V. Claude, L. Sacco, S.D. Lambert, Ethylene polymerization and hydrodechlorination of 1,2-dichloroethane mediated by nickel (II) covalently anchored to silica xerogels, *J. Sol-Gel Sci. Technol.* 81 (2017) 59–68. doi:10.1007/s10971-016-4272-0.
- [24] J.G. Mahy, V. Cerfontaine, D. Poelman, F. Devred, E.M. Gaigneaux, B. Heinrichs, et al., Highly efficient low-temperature N-doped TiO₂ catalysts for visible light photocatalytic applications, *Materials (Basel).* 11 (2018). doi:10.3390/ma11040584.
- [25] H. Benhebal, C. Wolfs, S. Kadi, R.G. Tilkin, B. Allouche, D. Lambert, et al., Visible Light Sensitive SnO₂/ZnCo₂O₄ Material for the Photocatalytic Removal of Organic

- Pollutants in Water, *Inorganics*. 7 (2019) 77.
- [26] J.P. Hill, L.K. Shrestha, S. Ishihara, Q. Ji, K. Ariga, Self-Assembly: From amphiphiles to chromophores and beyond, *Molecules*. 19 (2014) 8589–8609.
doi:10.3390/molecules19068589.
- [27] S.L. Burkett, M.E. Davis, Mechanism of Structure Direction in the Synthesis of Si-ZSM-5: An Investigation by Intermolecular ^1H - ^{29}Si CP MAS NMR, *J. Phys. Chem.* 98 (1994) 4647–4653.
- [28] Y. Kim, B. Lee, J. Yi, Synthesis of Mesoporous γ -Alumina through Pre- and Post-hydrolysis Methods, *Korean J. Chem. Eng.* 19 (2002) 908–910.
- [29] L. Wan, H. Fu, K. Shi, X. Tian, Simple synthesis of mesoporous alumina thin films, *Mater. Lett.* 62 (2008) 1525–1527. doi:10.1016/j.matlet.2007.09.046.
- [30] H.Y. Zhu, J.D. Riches, J.C. Barry, γ -Alumina nanofibers prepared from aluminum hydrate with poly(ethylene oxide) surfactant, *Chem. Mater.* 14 (2002) 2086–2093.
doi:10.1021/cm010736a.
- [31] J. Čejka, Organized mesoporous alumina: synthesis, structure and potential in catalysis, *Appl. Catal. A Gen.* 254 (2003) 327–338. doi:10.1016/S0926-860X(03)00478-2.
- [32] P. Kim, Y. Kim, H. Kim, I.K. Song, J. Yi, Synthesis and characterization of mesoporous alumina with nickel incorporated for use in the partial oxidation of methane into synthesis gas, *Appl. Catal. A Gen.* 272 (2004) 157–166.
doi:10.1016/j.apcata.2004.05.055.
- [33] P.F. Fulvio, R.I. Brosey, M. Jaroniec, Synthesis of mesoporous alumina from boehmite in the presence of triblock copolymer., *ACS Appl. Mater. Interfaces*. 2 (2010) 588–593. doi:10.1021/am9009023.

- [34] R. Bleta, P. Alphonse, L. Pin, M. Gressier, M.-J. Menu, An efficient route to aqueous phase synthesis of nanocrystalline γ -Al₂O₃ with high porosity: From stable boehmite colloids to large pore mesoporous alumina, *J. Colloid Interface Sci.* 367 (2012) 120–128. doi:10.1016/j.jcis.2011.08.087.
- [35] A. Afshar Taromi, S. Kaliaguine, Synthesis of ordered mesoporous Γ -alumina – Effects of calcination conditions and polymeric template concentration, *Microporous Mesoporous Mater.* 248 (2017) 179–191. doi:10.1016/j.micromeso.2017.04.040.
- [36] K. Ullmann, P. Ádám, K. Sinkó, Chemical tailoring of porous aluminum oxide xerogels, *J. Non. Cryst. Solids.* 499 (2018) 394–400. doi:10.1016/j.jnoncrysol.2018.07.044.
- [37] S. Tabesh, F. Davar, M.R. Loghman-Estarki, Preparation of γ -Al₂O₃ nanoparticles using modified sol-gel method and its use for the adsorption of lead and cadmium ions, *J. Alloys Compd.* 730 (2018) 441–449. doi:10.1016/j.jallcom.2017.09.246.
- [38] S. Rezaee, K. Ranjbar, A.R. Kiasat, The effect of surfactant on the sol–gel synthesis of alumina-zirconia nanopowders, *Ceram. Int.* 44 (2018) 19963–19969. doi:10.1016/j.ceramint.2018.07.263.
- [39] C. Italiano, N.T.J. Luchters, L. Pino, J. V. Fletcher, S. Specchia, J.C.Q. Fletcher, et al., High specific surface area supports for highly active Rh catalysts: Syngas production from methane at high space velocity, *Int. J. Hydrogen Energy.* 43 (2018) 11755–11765. doi:10.1016/j.ijhydene.2018.01.136.
- [40] V. Claude, M. Vilaseca, A.S. Tatton, C. Damblon, S.D. Lambert, Influence of the Method of Aqueous Synthesis and the Nature of the Silicon Precursor on the Physicochemical Properties of Porous Alumina, *Eur. J. Inorg. Chem.* 11 (2016) 1678–1689. doi:10.1002/ejic.201501383.

- [41] A. Lecloux, Exploitation des isothermes d'adsorption et de désorption d'azote pour l'étude de la texture des solides poreux, *Mémoires Société R. Des Sci. Liège.* (1971) 169–209.
- [42] J. Rouquérol, D. Avnir, C.W. Fairbridge, D.H. Everett, N. Pernicone, J.D. Ramsay, et al., Recommendations for the characterization of porous solids, *Pure Appl. Chem.* 66 (1994) 1739–1758.
- [43] V. Claude, J.G. Mahy, J. Geens, C. Courson, S.D. Lambert, Synthesis of Ni/ γ -Al₂O₃-SiO₂ catalysts with different silicon precursors for the steam toluene reforming, *Microporous Mesoporous Mater.* 284 (2019) 304–315.
doi:10.1016/j.micromeso.2019.04.027.
- [44] V. Claude, J.G. Mahy, J. Geens, S.D. Lambert, Ni-doped γ -Al₂O₃ as secondary catalyst for bio-syngas purification: influence of Ni loading, catalyst preparation, and gas composition on catalytic activity, *Mater. Today Chem.* 13 (2019) 98–109.
doi:10.1016/j.mtchem.2019.05.002.
- [45] S. Lambert, C. Cellier, F. Ferauche, E.M. Gaigneaux, B. Heinrichs, On the structure-sensitivity of 2-butanol dehydrogenation over CU/SiO₂ cogelled xerogel catalysts, *Catal. Commun.* 8 (2007) 2032–2036. doi:10.1016/j.catcom.2007.04.004.
- [46] S. Mani, J.R. Kastner, A. Juneja, Catalytic decomposition of toluene using a biomass derived catalyst, *Fuel Process. Technol.* 114 (2013) 118–125.
doi:10.1016/j.fuproc.2013.03.015.
- [47] I. Chorenorff, J.W. Niemantsverdriet, *Concepts o Modern Catalysis and Kinetics*, 2003. doi:10.1002/anie.200461440.
- [48] Z. Hao, Q. Zhu, Z. Jiang, B. Hou, H. Li, Characterization of aerogel Ni/Al₂O₃

- catalysts and investigation on their stability for CH₄-CO₂ reforming in a fluidized bed, *Fuel Process. Technol.* 90 (2009) 113–121. doi:10.1016/j.fuproc.2008.08.004.
- [49] J. Guo, H. Lou, H. Zhao, D. Chai, X. Zheng, Dry reforming of methane over nickel catalysts supported on magnesium aluminate spinels, *Appl. Catal. A Gen.* 273 (2004) 75–82. doi:10.1016/j.apcata.2004.06.014.
- [50] M. Ito, T. Tagawa, S. Goto, Suppression of carbonaceous depositions on nickel catalyst for the carbon dioxide reforming of methane, *Appl. Catal. A Gen.* 177 (1999) 15–23.
- [51] L. Garcia, R. French, S. Czernik, E. Chornet, Catalytic steam reforming of bio-oils for the production of hydrogen: effects of catalyst composition, *Appl. Catal. A Gen.* 201 (2000) 225–239.
- [52] G. Guan, G. Chen, Y. Kasai, E.W.C. Lim, X. Hao, M. Kaewpanha, et al., Catalytic steam reforming of biomass tar over iron- or nickel-based catalyst supported on calcined scallop shell, *Appl. Catal. B Environ.* 115–116 (2012) 159–168. doi:10.1016/j.apcatb.2011.12.009.
- [53] A.M. da Silva, L.O.O. da Costa, K.R. Souza, L. V. Mattos, F.B. Noronha, The effect of space time on Co/CeO₂ catalyst deactivation during oxidative steam reforming of ethanol, *Catal. Commun.* 11 (2010) 736–740. doi:10.1016/j.catcom.2010.02.005.
- [54] C.N. Satterfield, *Mass transfer in heterogeneous catalysis*, Cambridge, 1970.

Figure 1: Synthesis methods for the preparation of Ni/ γ -Al₂O₃ catalysts: (A) pure Ni/ γ -Al₂O₃ and (B to E) modified with stearic acid.

Figure 2: TEM observations of calcined Ni/ γ -Al₂O₃ catalysts: (a) Ni10/Al₂O₃-A; (b) Ni10/Al₂O₃-B; (c) Ni10/Al₂O₃-C; (d) Ni10/Al₂O₃-D and (e) Ni10/Al₂O₃-E.

Figure 3: Nitrogen adsorption-desorption isotherms and mesopore size distribution for Ni/ γ -Al₂O₃ catalysts synthesized with stearic acid.

Figure 4: Proposed mechanism explaining the differences between samples prepared by method “B” or by method “D”.

Figure 5: Sizes of the metallic Ni particles as a function of microporous volume for 10 wt. % Ni/ γ -Al₂O₃ samples modified with stearic acid after H₂ reduction or after TPR measurements.

Figure 6: TPR profiles of 10 wt. % Ni/ γ -Al₂O₃ catalysts synthesized with stearic acid; (×) Ni10/Al₂O₃-A, (■) Ni10/Al₂O₃-D, (◆) Ni10/Al₂O₃-E, (●) Ni10/Al₂O₃-B, (▲) Ni10/Al₂O₃-C.

Figure 7: SEM pictures of (a) Ni10/Al₂O₃-A and (b-c) Ni10/Al₂O₃-C samples.

Figure 8: Mercury porosimetry curves (left side) and macropore size distribution determined from mercury porosimetry measurements (right side) for Ni10/Al₂O₃-A and Ni10/Al₂O₃-C samples.

Figure 9: Toluene conversion as a function of time for Ni10/Al₂O₃-A and Ni10/Al₂O₃-C catalysts.

Figure 10: Post-test DSC curves for: (■) Ni10/Al₂O₃-A and (▲) Ni10/Al₂O₃-C samples.

Figure 11: Influences of the morphology on the catalytic activity and coking between samples Ni10/Al₂O₃-A and Ni10/Al₂O₃-C.

Table 1: Composition, Textural properties and particle sizes of samples.

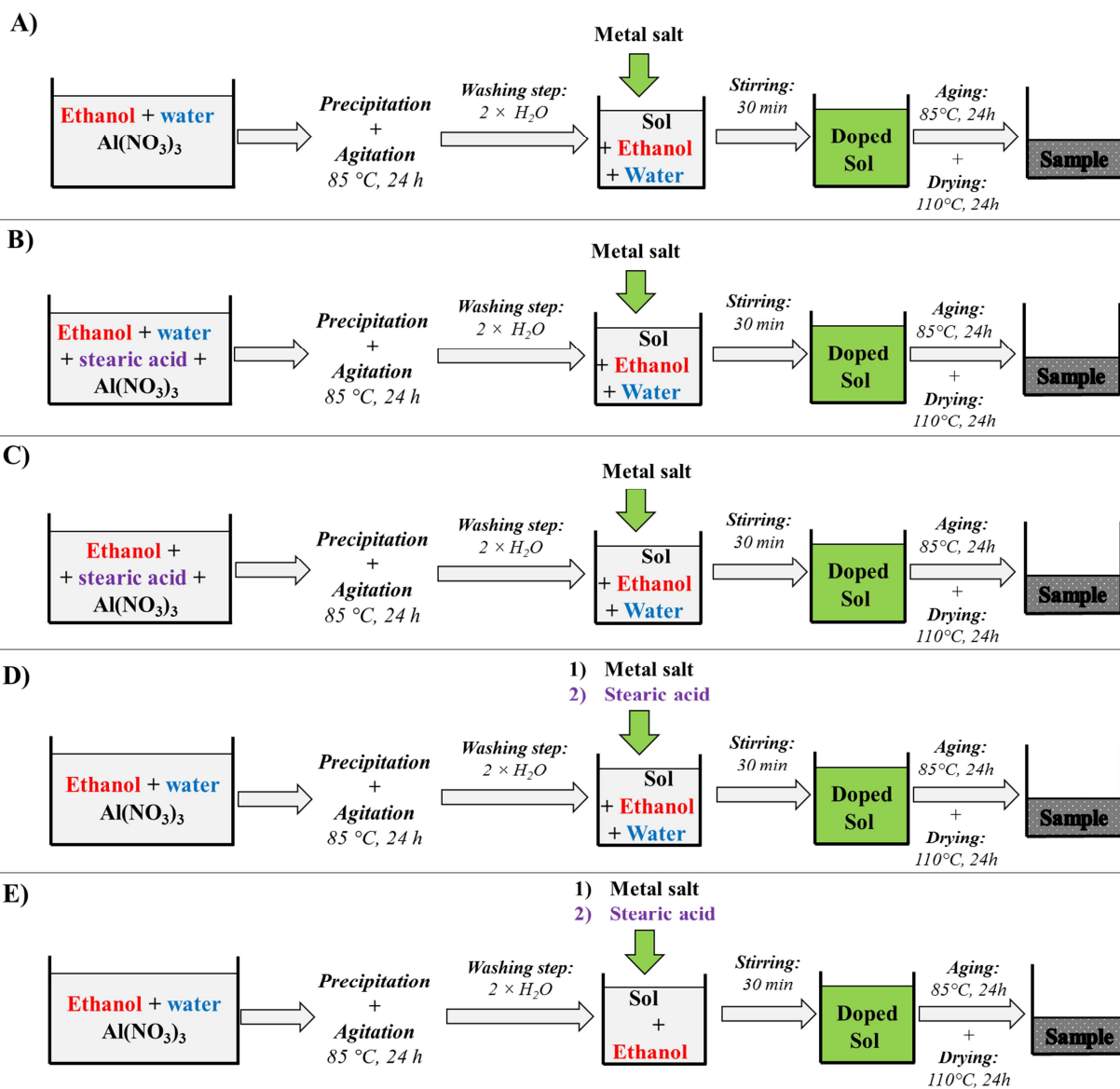
Sample	Al ₂ O ₃		Ni		<i>S</i> _{BET} (m ² /g)	<i>V</i> _p (cm ³ /g)	<i>V</i> _{DR} (cm ³ /g)	After reduction			After TPR		<i>V</i> _{Hg} (cm ³ /g)	ρ (g/cm ³)	ρ_{Eff} (g/cm ³)
	Theo. (wt%)	Exp. (wt%) ± 0.1	Theo. (wt%)	Exp. (wt%) ± 0.1				<i>d</i> _{TEMNi} (nm)	<i>d</i> _{XRDNi} (nm) ± 1	<i>d</i> _{XRD,Al₂O₃} (nm) ± 1	<i>d</i> _{TEMNi} (nm)	<i>d</i> _{XRDNi} (nm) ± 1			
Ni10/Al ₂ O ₃ -A	90.0	89.5	10.0	10.5	240	0.3	0.08	8 ± 2	9	5.4	30 ± 9	23	< 0.1	3.0	0.7
Ni10/Al ₂ O ₃ -B	90.0	88.7	10.0	11.3	315	0.8	0.13	5 ± 1	6	5.6	16 ± 6	16	-	-	-
Ni10/Al ₂ O ₃ -C	90.0	89.2	10.0	11.1	330	0.9	0.12	7 ± 1	7	5.5	24 ± 6	19	0.9	3.1	0.2
Ni10/Al ₂ O ₃ -D	90.0	90.2	10.0	9.8	280	0.5	0.10	7 ± 2	10	5.6	28 ± 12	21	-	-	-
Ni10/Al ₂ O ₃ -E	90.0	89.6	10.0	10.4	275	0.7	0.09	8 ± 2	8	5.4	28 ± 14	24	-	-	-

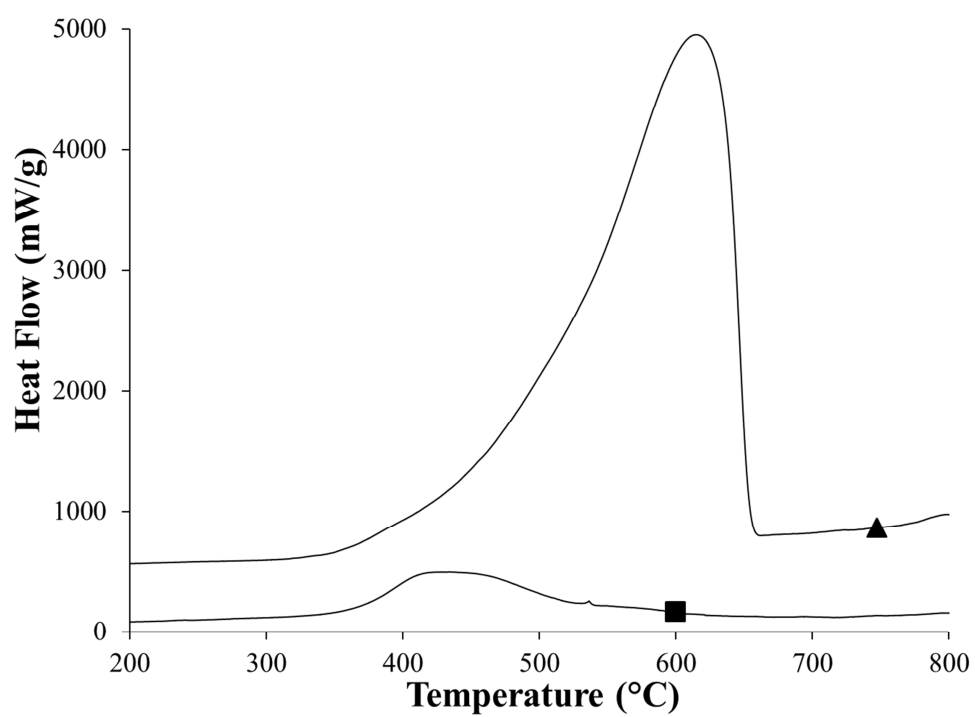
*S*_{BET}: specific surface area; *V*_p: porous volume; *V*_{DR}: microporous volume, *d*_{TEMNi}: Ni particles size measured by TEM; *d*_{XRDNi}: metallic nickel crystallites size estimation made by XRD on the Ni (2 0 0) ray; *d*_{XRD,Al₂O₃}: γ -Al₂O₃ crystallites size determined by XRD on the (4 4 0) ray; *V*_{Hg}: macroporous volume determined by mercury porosimetry measurements; ρ : apparent density determined by helium pycnometry; ρ_{Eff} : effective density determined by the density of the catalysts bed and a close-packing of 0.74.

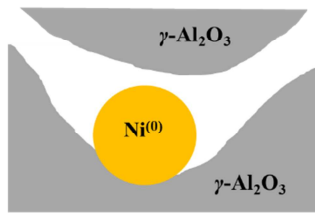
Table 2: Catalytic performances for Ni10/Al₂O₃-A and Ni10/Al₂O₃-C samples. Test conditions: 650 °C, 300 min, 24.000 ppmv of toluene, GHSV of 5000 h⁻¹.

Sample	d_{TEMNi} (nm)	d_{XRDNi} (nm)	C_{T} (%)	r_{T} (mol _{Tolu} /(g _{Ni} ·h))	S_{B} (%)	<i>Coke</i> (g _{Carbon} /g _{Cata})	<i>Coke*</i> (g _{Carbon} /g _{Tolu})	<i>Fil. carbon</i>
Ni10/Al ₂ O ₃ -A	11 ± 3	12 ± 1	51	6.7 · 10 ⁻²	15	0.10	3.1 · 10 ⁻²	+
Ni10/Al ₂ O ₃ -C	15 ± 7	13	42	1.4 · 10 ⁻¹	12	1.35	2.0 · 10 ⁻¹	+++

d_{TEMNi} : metallic particles size measured by TEM; d_{XRDNi} : metallic crystallites size estimation obtained by XRD. C_{T} : conversion of toluene, r_{T} : reaction rate of toluene, S_{B} : benzene selectivity. *Coke*: carbon deposit amount after 5 h of test measured by TG-DSC, *Coke**: tendency of sample to form carbon deposit.





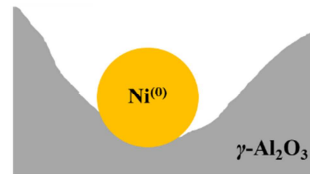
a) Ni10/Al₂O₃-A

- $\Phi \ll 1$: No diffusional limitations of the reagents;
 - However: lower diffusion rate of reagents than for Ni10/Al₂O₃-C;
- ⇒ Similar to a decrease of *GHSV*

So:

$$r_{T,ads.+crack.} \sim r_{gasification}$$

⇒ **Low tendency to form coke**

b) Ni10/Al₂O₃-C

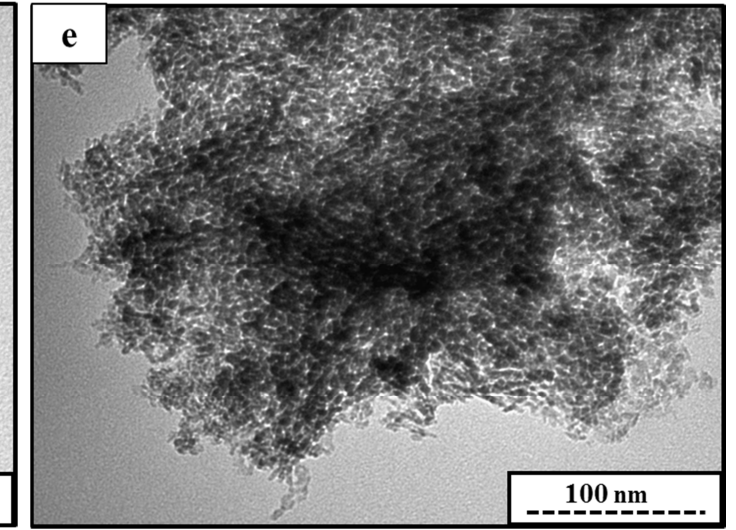
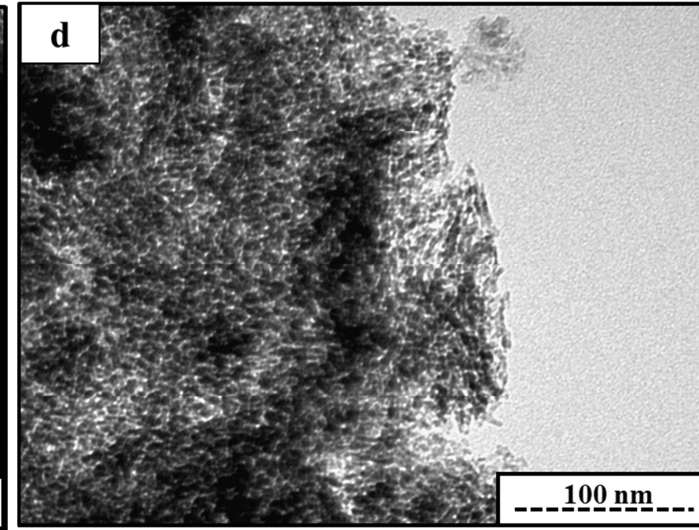
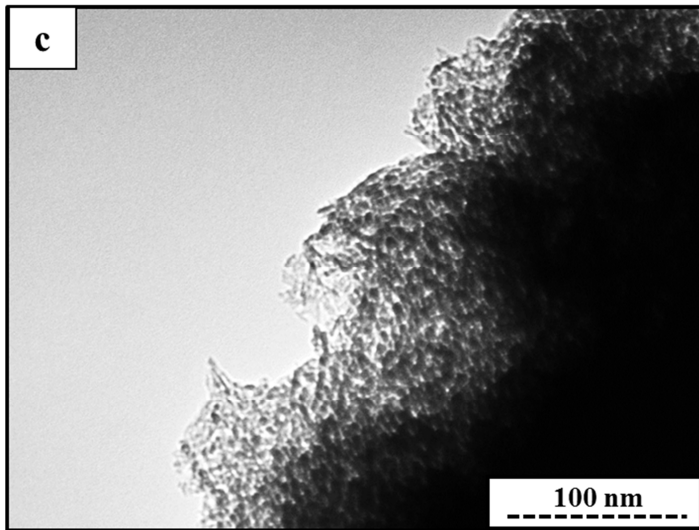
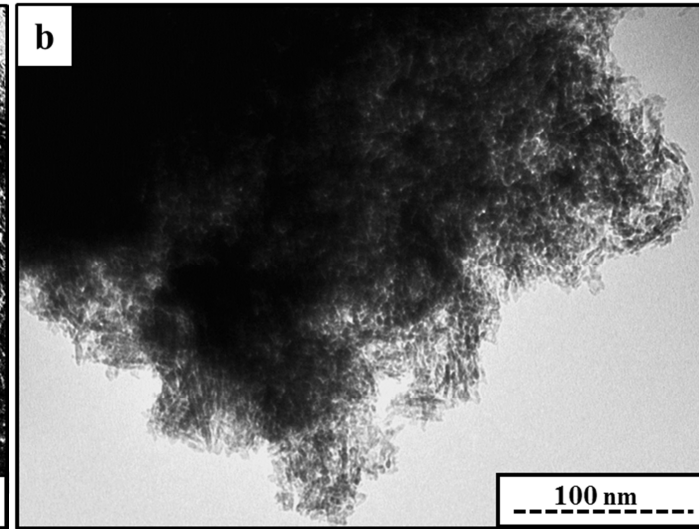
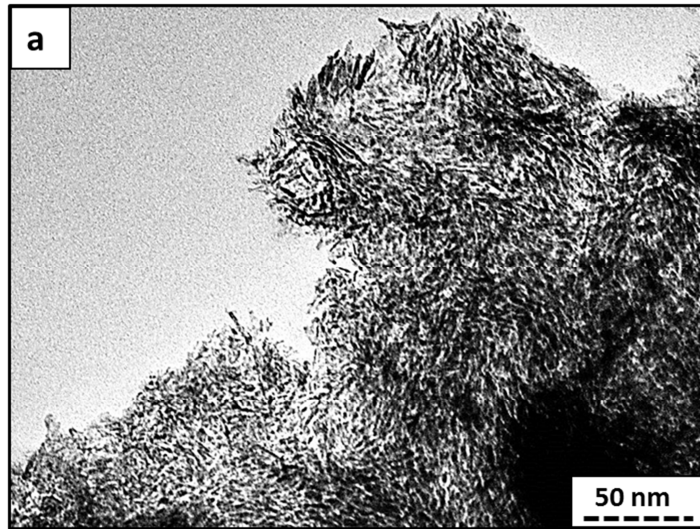
- $\Phi \ll 1$: No diffusional limitations of the reagents
 - However: higher diffusion rate of reagents than for Ni10/Al₂O₃-A;
- ⇒ Similar to an increase of *GHSV*

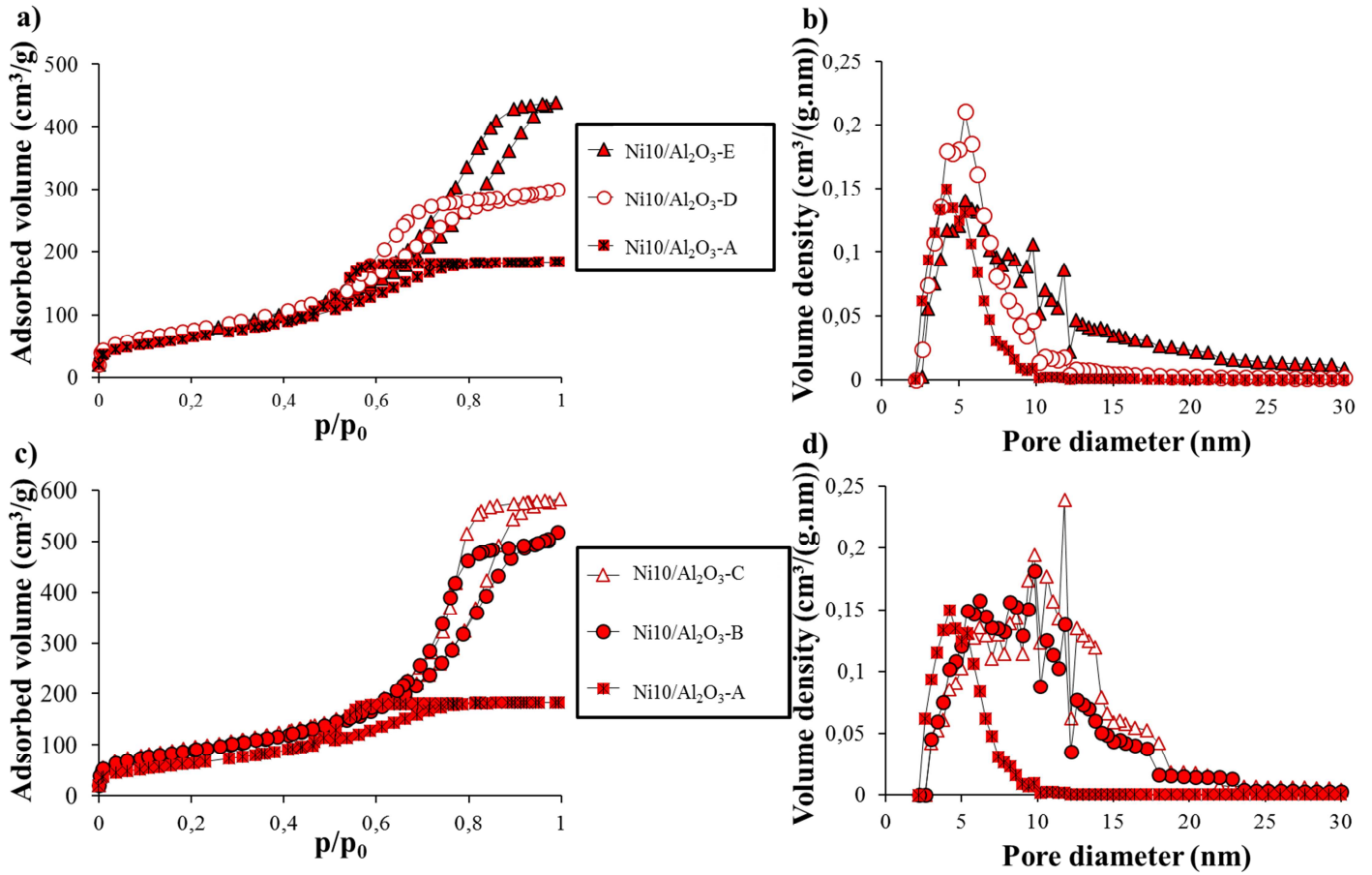
So:

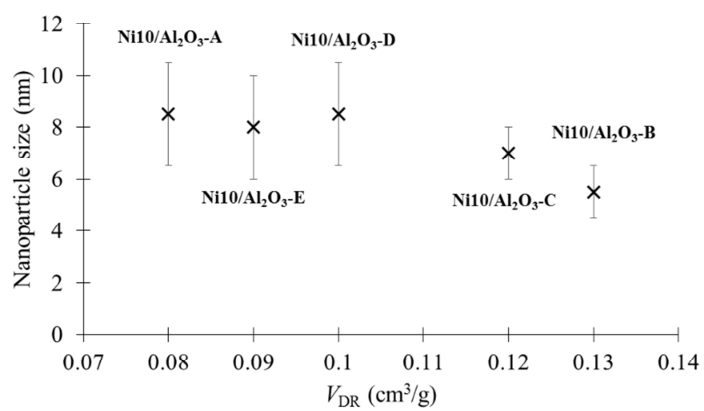
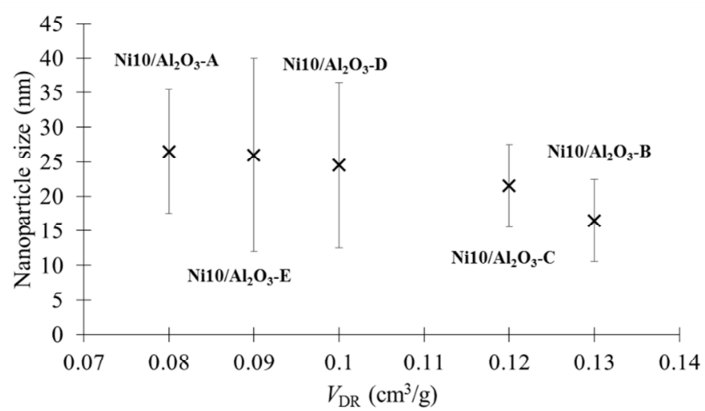
$$r_{T,ads.+crack.} \gg r_{gasification}$$

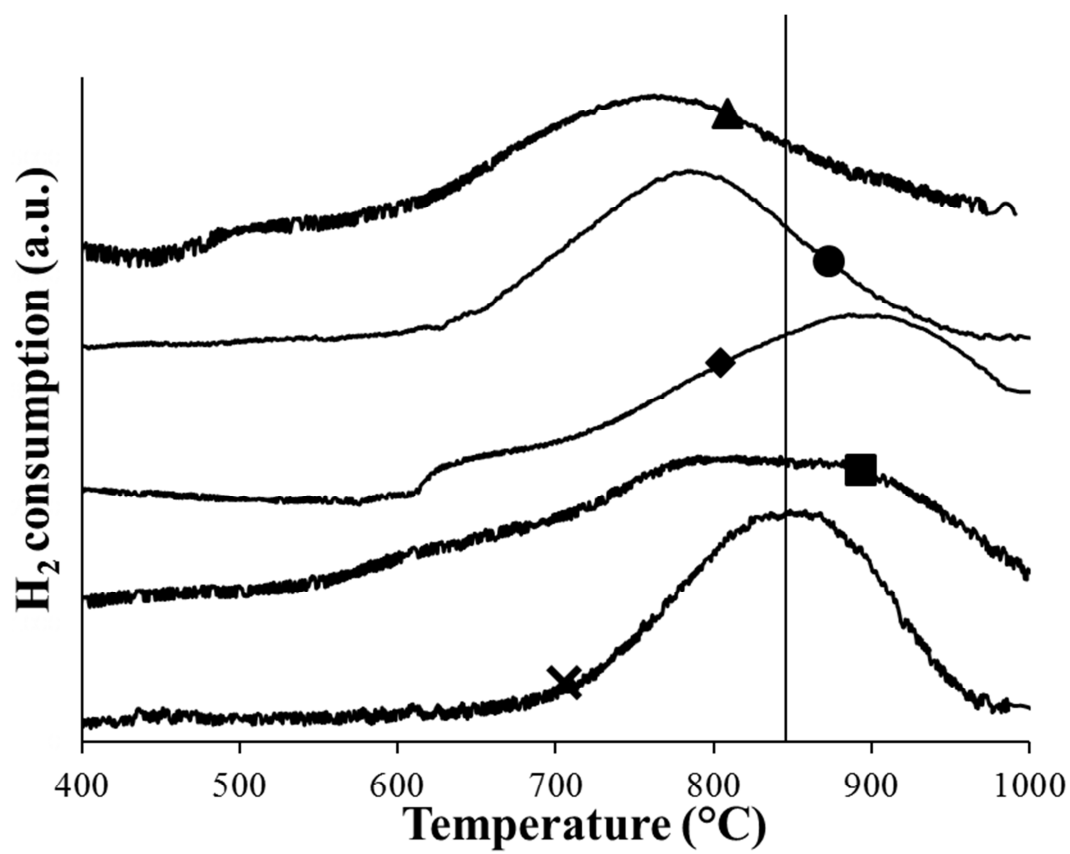
⇒ **High tendency to form coke**

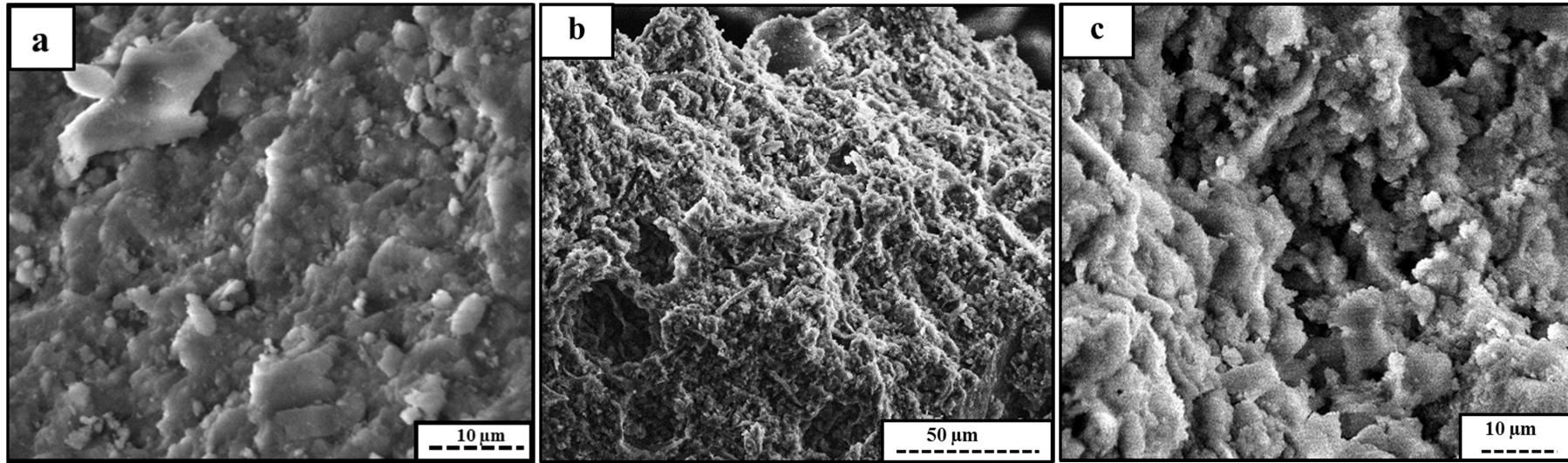
Journal Pre-proof

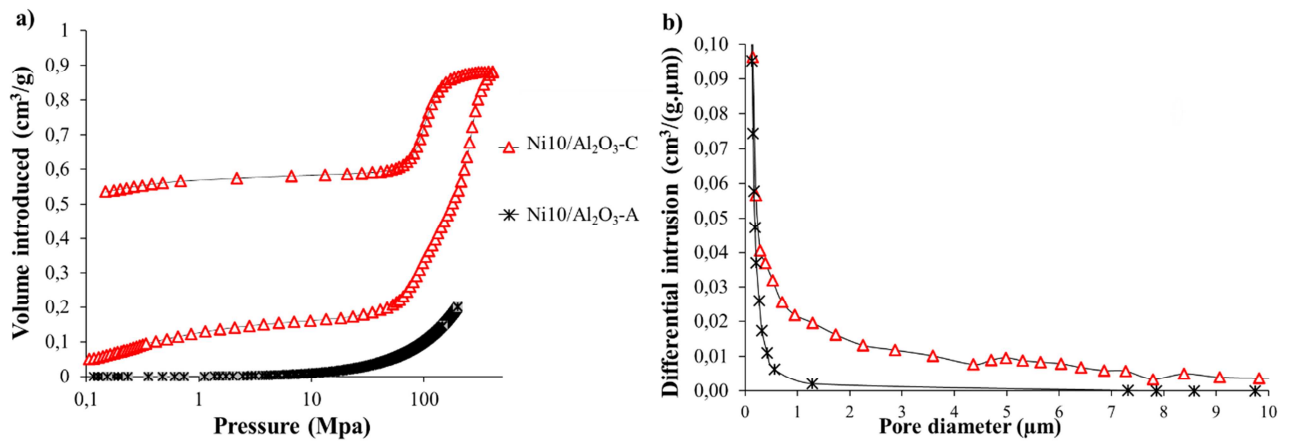


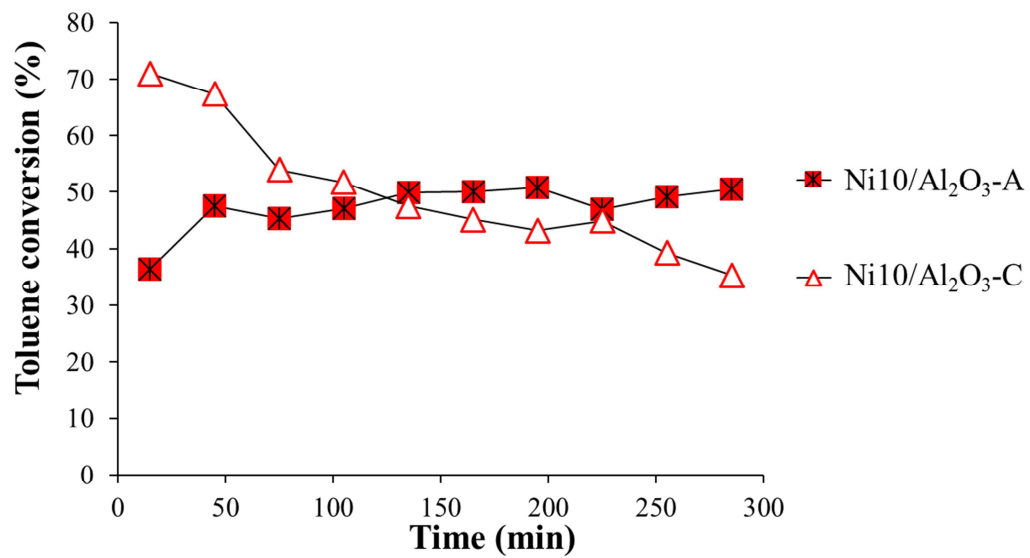


a) After reduction**b) After TPR**









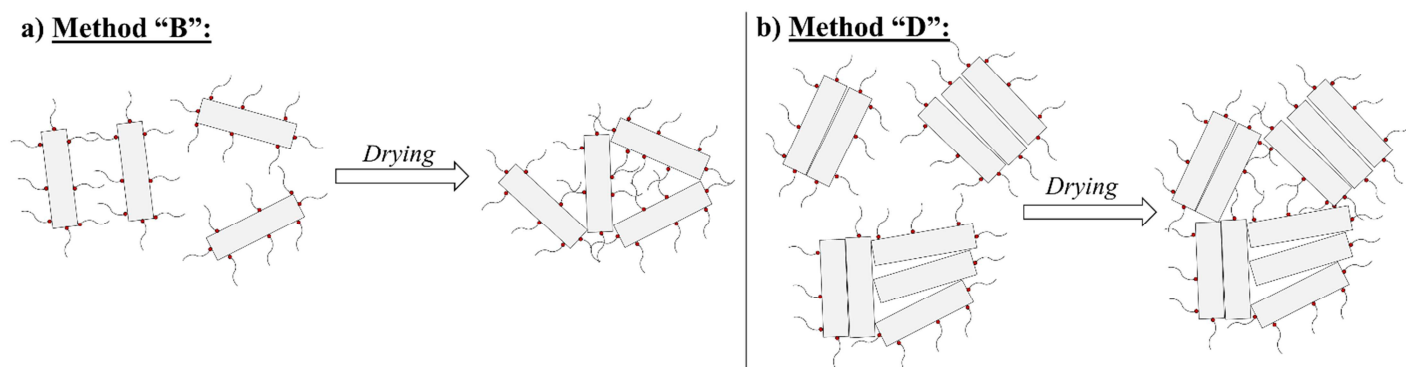


Figure 4: Proposed mechanism explaining the differences between samples prepared by (a) method "B" or by (b) method "D".

- Sol-gel preparation of Ni/ γ -Al₂O₃ catalysts.
- Modifications of γ -Al₂O₃ supports with stearic acid.
- Catalyst texture influenced by the step of addition of the surfactant.
- Reducibility of the catalysts influenced by textural modification.
- Toluene conversion increased with tailoring.

Journal Pre-proof